



Porous nitrogen-rich g-C₃N₄ nanotubes for efficient photocatalytic CO₂ reduction

Zhao Mo^a, Xingwang Zhu^a, Zhifeng Jiang^a, Yanhua Song^b, Daobin Liu^c, Hongping Li^a, Xiaofei Yang^d, Yuanbin She^e, Yucheng Lei^a, Shouqi Yuan^a, Huaming Li^a, Li Song^c, Qingyu Yan^f, Hui Xu^{a,*}

^a School of Materials Science & Engineering, Institute for Energy Research, Jiangsu University, Zhenjiang 212013, PR China

^b School of Environmental and Chemical Engineering, Jiangsu University of Science and Technology, Zhenjiang 212003, PR China

^c National Synchrotron Radiation Laboratory, University of Science and Technology of China, Hefei 230029, PR China

^d School of Science, Institute of Materials Physics and Chemistry, Nanjing Forestry University, Nanjing 210037, PR China

^e College of Chemical Engineering, Zhejiang University of Technology, Hangzhou 310014, PR China

^f School of Materials Science and Engineering, Nanyang Technological University, 50 Nanyang Avenue, Singapore 639798, Singapore

ARTICLE INFO

Keywords:

g-C₃N₄ nanotubes
Photocatalytic CO₂ reduction
Supramolecular self-assembly
Nitrogen-rich

ABSTRACT

The conversion of carbon dioxide (CO₂) into fuels and valuable chemicals using solar energy is a promising method for reducing CO₂ emissions and solving energy supply issues. However, the development of inexpensive, efficient and metal-free materials for photocatalytic CO₂ reduction is challenging. Herein, we report a facile supramolecular self-assembly strategy for the preparation of porous nitrogen-rich graphitic carbon nitride (g-C₃N₄) nanotubes with Lewis basicity and a large surface area, which are beneficial for the adsorption of CO₂ and, consequently, the enhancement of the photocatalytic CO₂ reduction activity. The metal-free porous nitrogen-rich g-C₃N₄ nanotubes catalyst exhibits a superior visible-light-induced CO₂-to-CO conversion rate of 103.6 μmol g⁻¹ h⁻¹, which is 17 and 15 times higher than those of bulk g-C₃N₄ (6.1 μmol g⁻¹ h⁻¹) and P25-TiO₂ (7.1 μmol g⁻¹ h⁻¹), respectively, and exceeds the performance of most metal-free photocatalysts. This work provides new insights into the synthesis of functional groups-modified g-C₃N₄ with a unique structure for effective photocatalytic CO₂ reduction.

1. Introduction

The increasing consumption of fossil fuel along with massive emission of carbon dioxide (CO₂) has caused an intractable energy and environmental crisis [1–4]. The photocatalytic conversion of CO₂ into hydrocarbon fuels represents a promising strategy to combat this crisis [5–8]. To date, numerous semiconductors have been applied for the light-driven photoreduction of CO₂, such as metal sulfides [9], metal oxides [10] and other metal-based composites [11]. However, the CO₂ conversion efficiency of these semiconductors is still unsatisfactory, mainly because of the weak adsorption of CO₂ and rapid rate of charge carrier recombination [12,13]. To address these shortcomings, new types of metal-free photocatalysts including black phosphorus (BP) [5], graphitic carbon nitride (g-C₃N₄) [14–16], boron carbon nitride (BCN) [17,18] and boron carbide (BC) have been developed to increase the specific surface area and the number of active sites to yield practical catalysts [19]. Achieving high-efficiency CO₂ conversion relies on the

presence of a suitable structure, including different spatial dimensions [20]. In particular, nanotube structures are often used as one-dimensional (1D) materials for photocatalytic CO₂ reduction, this is because of their special structural advantages, such as the high concentration of wall-exposed active sites, which speeds up the adsorption of CO₂ and increases the efficiency of photogenerated electron and hole separation by reducing the diffusion distance from the bulk to the interface [21,22].

1D materials can be synthesized via the hard-templating and soft-templating methods, however the above methods have obvious disadvantages such as poor structure stability, complicated steps and the utilization of environment-hazardous solvent [23,24]. As a result, a simple, environment friendly, effective and stable method is urgently needed to prepare 1D materials. Coincidentally, supramolecular assembly methods have unique advantages for the synthesis of 1D materials because they are based on noncovalent interactions (hydrogen bonding, van der Waals forces and π–π stacking), which allow the self-assembly

* Corresponding author.

E-mail address: xh@ujs.edu.cn (H. Xu).

<https://doi.org/10.1016/j.apcatb.2019.117854>

Received 22 February 2019; Received in revised form 14 May 2019; Accepted 9 June 2019

Available online 11 June 2019

0926-3373/ © 2019 Elsevier B.V. All rights reserved.

of π -conjugated molecules into well-defined 1D nanomaterials without outside guidance or management [25]. In past years, numerous π -conjugated molecules have been used to the controlled synthesis of 1D ordered polymer semiconductors through supramolecular self-assembly [26]. Among them, 1D $g\text{-C}_3\text{N}_4$ has been extensively applied for photocatalytic field due to its 1D tubular structure and superior photocatalytic performance [27,28]. The construction of 1D $g\text{-C}_3\text{N}_4$ by supramolecular self-assembly is a good strategy because supramolecular self-assembly results in organic molecules forming larger aggregates and controlled crystal growth via hydrogen bonding interactions, ultimately yielding well-ordered $g\text{-C}_3\text{N}_4$ via a self-templating method [29–33]. Meanwhile, heteroatom functional groups can be introduced into $g\text{-C}_3\text{N}_4$ by the selection of suitable organic molecules [34–37].

Herein, we report the preparation of porous nitrogen-rich $g\text{-C}_3\text{N}_4$ nanotubes ($\text{TCN}(\text{NH}_3)$) via supramolecular self-assembly. This material shows excellent visible light-driven CO_2 reduction performance compared to those of bulk $g\text{-C}_3\text{N}_4$ and other carbon-based photocatalysts. The outstanding photocatalytic CO_2 reduction performance can be attributed to the following factors: (i) the regular hollow, porous and 1D tubular structure boosts the charge separation efficiency and provides abundant active sites for the surface reaction, (ii) the modification with amino groups not only prolongs the lifetime of the excited charges but also results in strong Lewis basicity, which is beneficial for CO_2 adsorption, thus promoting the CO_2 photoreduction reaction [15,38–45].

2. Results and discussion

2.1. Formation process of $\text{TCN}(\text{NH}_3)$

The synthesis of $\text{TCN}(\text{NH}_3)$ is shown schematically in Fig. 1a. First, to effectively regulate the intermediate, which has a significant effect on the electronic structure and photocatalytic activity of the final carbon nitride material [24,46], supramolecular self-assembly was carried out with melamine and hydroxylammonium chloride as precursors by hydrothermal method at 120°C . The hydroxylammonium

chloride provides many amino and hydroxyl groups for the formation of a supramolecular intermediate through hydrogen bonds with the amino groups of melamine during hydrothermal reaction. As shown in Fig. 1, the melamine, which has a relatively irregular morphology (Fig. S1a), is transformed into 200 nm regular nanorods (the supramolecular intermediate, Fig. 1b and S1b, c) after hydrothermal reaction. This is not just a simple change in morphology but also a fundamental change in the chemical structure that can be demonstrated by X-ray diffraction (XRD) and Fourier transform infrared (FT-IR) analyses (Fig. S1d, e). As shown in Fig. S1d, the peaks of the supramolecular intermediate are obviously different from those of melamine, two main peaks at 10.6° and 27.5° correspond to the periodic arrays of intraplanar stacking and interlayer aromatic stacking [29], which indicates that the chemical structure of melamine has been fundamentally changed and transformed into the supramolecular intermediate. As shown in Fig. S1e, the peak positions of supramolecular intermediate are different from that of bulk $g\text{-C}_3\text{N}_4$, which may be attributed to the hydrogen-bonded network in supramolecular intermediate. This conclusion can be further confirmed by FT-IR analysis (Fig. S1f). Meanwhile, the result of X-ray photoelectron spectroscopy (XPS) survey spectra in Fig. S2 reveals that the O content of supramolecular intermediate is far higher than that of bulk $g\text{-C}_3\text{N}_4$, which can be ascribed to the hydrogen-bonded network in supramolecular intermediate. To prepare $\text{TCN}(\text{NH}_3)$, the supramolecular intermediate was subsequently heated under an NH_3 atmosphere. Interestingly, the $\text{TCN}(\text{NH}_3)$ sample exhibits a 1D tubular structure with a length of 2–3 μm and a diameter of 30–60 nm (Fig. 1c, d). However, the bulk $g\text{-C}_3\text{N}_4$ derived from melamine comprises large and irregular grains (Fig. S3a). The magnified transmission electron microscopy (TEM) image shown in Fig. 1e further reveals that abundant pores are distributed in the 1D tubular structure. The 1D tubular structure and abundant pores contribute to increasing the number of photogenerated electrons outside the nanotubes, as well as light harvesting and CO_2 transmission/adsorption [29,37,47]. The chemical element mappings of $\text{TCN}(\text{NH}_3)$ demonstrate that C and N are homogeneously distributed over the 1D tubular structure (Fig. 1f–h). Meanwhile, the edge of the 1D

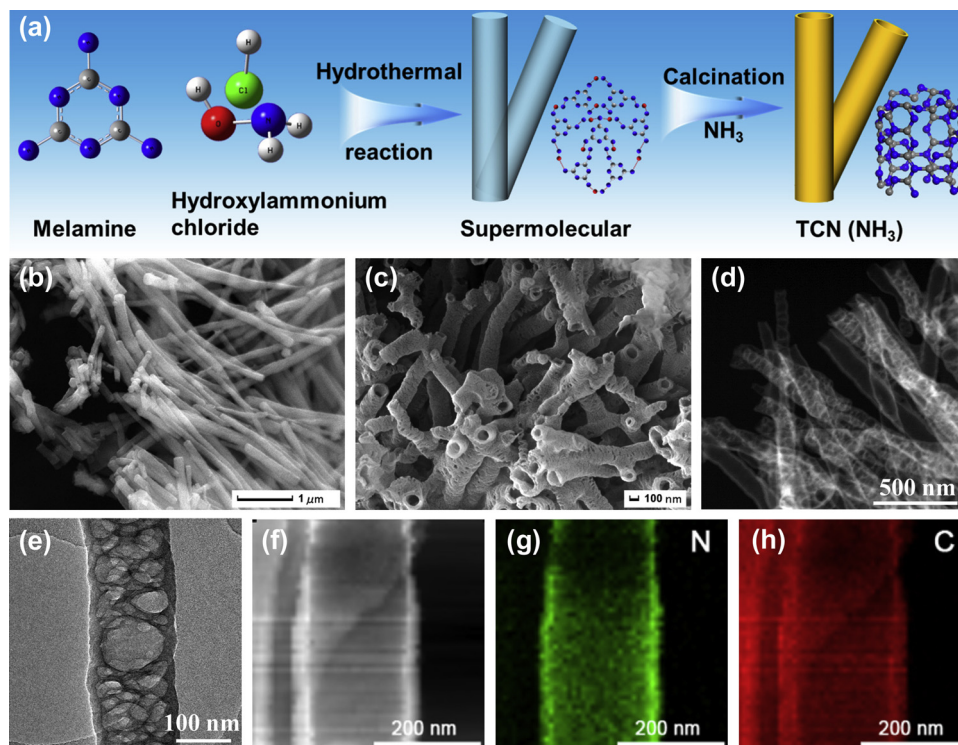


Fig. 1. Formation and characterization of $\text{TCN}(\text{NH}_3)$. (a) Schematic illustration of the synthetic process, (b, c) SEM images, (d, e) TEM images, (f) scanning tunneling electron microscopy (STEM) image and (g, h) energy dispersive X-ray (EDX) maps of the $\text{TCN}(\text{NH}_3)$.

structure has higher concentrations of C and N, which is a typical characteristic of tubular structure. The Brunauer-Emmett-Teller (BET) surface area of TCN(NH₃) is 135.8 m² g⁻¹, which is larger than that of bulk g-C₃N₄ (8.6 m² g⁻¹) (Fig. S3d). The high surface area of TCN (NH₃) can be mainly attributed to the unique 1D tubular structure and abundant pores. The scanning electron microscopy (SEM) analysis indicates that TCN(NH₃) prepared under an increasing NH₃ flow rate results in the following changes (Fig. S4): as the flow rate increases, the porous nanotube structure is gradually formed, but, when the NH₃ flow rate exceeds 400 mL/min, the nanotube structure is destroyed. The possible reason is that the multi-layer g-C₃N₄ nanotubes are gradually etched by NH₃, eventually leading to the collapse of the nanotube structure. NH₃ etching plays an important role in the synthesis of ultrathin g-C₃N₄ [48,49]. Fig. S5 shows SEM images of the TCN synthesized in different atmosphere (Air, Ar, N₂ and NH₃), which all exhibits 1D tubular structure. As shown in Fig. S6 and 1 e, the clearer features of the pores in 1D tubular structure are further analyze by TEM images of the TCN synthesized in different atmosphere (Air, Ar, N₂ and NH₃). No obvious pores are observed in the TCN(Air), TCN(Ar) and TCN(N₂) samples, but conversely abundant pores are distributed in the 1D tubular structure of TCN(NH₃). Thus, the porous structure can only be obtained by preparation under an NH₃ atmosphere.

As shown in Fig. S3b, the bulk g-C₃N₄ exhibits two distinctive peaks at 27.3° and 13.1°, which can be assigned to the interlayer stacking of conjugated aromatic rings and the in-plane structured tri-s-triazine units, respectively [50,51]. Compared to that of the bulk g-C₃N₄, the peak located at 13.1° of TCN(NH₃) becomes much weaker, indicating that the in-plane tri-s-triazine units are damaged [48]. In addition, the peak at 27.3° becomes weaker and broader, indicating the size-dependent properties of the 1D tubular structure. As shown in the FT-IR spectra (Fig. S3c), TCN(NH₃) maintains a typical g-C₃N₄ structure. In detail, the peak at 812 cm⁻¹ is due to the vibration mode of the s-triazine units [52,53]. The multiple bands at 1242, 1327, 1413 and 1641 cm⁻¹ are attributed to the typical vibration modes of C–N heterocycles [54]. The broad band between 3000 and 3600 cm⁻¹ corresponds to the stretching modes of –NH_x moieties [55]. The broad band of TCN(NH₃) shifts left compared to that of the bulk g-C₃N₄ and the intensity of amino groups is also enhanced (the inset of Fig. S3c), which indicates that more amino groups are grafted into the porous g-C₃N₄ nanotubes during the polymerization of the supramolecular intermediate under an NH₃ atmosphere [55–58]. The XRD patterns and FT-IR spectra of the TCN catalysts synthesized under different conditions and atmospheres are shown in Fig. S7. The results indicate that the synthesized materials maintain the carbon nitride structure well.

To confirm the fine structure of TCN(NH₃), elemental analysis (EA), X-ray absorption near edge structure (XANES) and XPS measurements were carried out [59–61]. As shown by the EA analysis (Table S1), the C/N atomic ratio of TCN(NH₃) is significantly lower than those of TCN samples synthesized under other atmospheres, which indicates that more N has been introduced into the TCN(NH₃). XANES analysis is an effective technique to analyze the local atomic and electronic structures of the TCN(NH₃) samples. As shown in Fig. 2, the XANES C K-edge and N K-edge spectra indicate that the TCN(NH₃) retains the tri-s-triazine-based structure of bulk g-C₃N₄. In the C K-edge spectra (Fig. 2a), three main features can be ascribed to the π* excitations of out-of-plane C=C bonds (ca. 285.5 eV) and C–N–C bonds (ca. 288.4 eV) and the σ* excitations of C–N–C/C–N bonds (> 293 eV) [62]. More careful examination of the C K-edge spectra shows that the intensity of the π*_{C=C} feature decreases after treatment with NH₃. This may be attributed to the etching effect of ammonia on the host framework, which weakens the interlayer bonding of the TCN(NH₃) [48]. The SEM and TEM images (Fig. 1) also show the 1D tubular and surface porous structure of TCN (NH₃). Moreover, the increased intensity of the π*_{C–N–C} feature in the spectrum of TCN(NH₃) compared to that in the spectrum of the bulk counterpart is observed, implying significant formation of the C–N–C structure on NH₃ etching. This phenomenon can be more clearly seen in

the C 1s XPS spectra (Fig. 2c and Table S3). The N K-edge XANES and N 1s XPS spectra for both materials are also collected and presented in Fig. 2b, d and Table S4. In the π* region, two sharp and intense peaks are observed at ca. 399.7 and 402.5 eV; these correspond to the aromatic C–N–C coordination in heterocyclic rings and sp³ N-3C bridging between tri-s-triazine, respectively. A weak shoulder peak centered at ca. 401.4 eV may be derived from graphitic three-fold nitrogen species (N-3C) [63]. The broad feature at > 405 eV is attributed to the σ* excitation of C–N–C or C–N bonds. The π*_{C–N–C} feature shows obviously increased intensity, which is consistent with the results obtained from the C K-edge spectra. Meanwhile, a slightly decreased intensity of the π*_{N-3C} peak suggests that the N-3C bonds in the g-C₃N₄ framework could be partially broken. Based on the above-mentioned results, we conclude that the TCN(NH₃) is mainly formed by the opening of the C–N bonds in the reduced NH₃ atmosphere, resulting in more amino defects with terminal isolated amino groups.

2.2. Photocatalytic CO₂ reduction performance

To explore the effect of the porous 1D tubular structures and abundant amino groups on the photocatalytic performance, photocatalytic CO₂ reduction experiments were conducted under irradiation with a 300-W Xe lamp. The predominant reaction products are CO and a trace amount of H₂. As shown in Fig. 3a, the bulk g-C₃N₄ only shows feeble CO₂ reduction performance, having a CO generation rate of 6.1 μmol g⁻¹ h⁻¹. Once TCN samples are formed after calcination under different atmospheres, the CO₂ reduction performance is substantially improved. One of the important reasons for this improvement is the larger surface area (Table S5) [64,65]. In particular, compared with those of the TCN(Air), TCN(Ar) and TCN(N₂) samples, the TCN (NH₃) catalyst has higher photocatalytic performance. A CO generation rate of 103.6 μmol g⁻¹ h⁻¹ is achieved for the TCN(NH₃) sample, which is 17.0, 1.8, 2.7 and 2.8 times higher than those of bulk g-C₃N₄, TCN (Air), TCN(Ar) and TCN(N₂), respectively. To study the photocatalytic CO₂ reduction of TCN(NH₃) further, a series of photocatalytic reduction experiments for TCN(NH₃) calcined with different NH₃ flow rates were investigated. As shown in Fig. 3b, the photocatalytic activity of the TCN (NH₃) materials first increased and then decreased as the flow rate increased. The CO generation rates are 66.8, 73.5, 103.6 and 86.5 μmol g⁻¹ h⁻¹ for the samples prepared under NH₃ flow rates of 50, 100, 200 and 400 mL/min, respectively. The TCN(NH₃) sample calcined under NH₃ at 200 mL/min showed the highest CO production rate. Experiments with ¹³C isotopic labeling were performed to provide direct evidence of the carbon source of the generated CO [66], as shown in Fig. 4a, b. The gas chromatography-mass spectrometry (GC-MS) spectral analysis reveals that the reduction product is ¹³CO₂ after photoreduction using the TCN(NH₃) catalyst, where the strong signal in the MS spectrum at m/z = 29 is designated as ¹³CO. This result provides strong evidence that the formed CO originates from CO₂ molecules. In the absence of TCN(NH₃), almost no CO is generated (Fig. 3c, column 2). In addition, as shown in Fig. 3c, column 3, no products are observed under dark conditions, indicating the photocatalytic nature of the CO₂ reduction reaction. When CO₂ is replaced with Ar, no CO is detected and only a little H₂ is generated (Fig. 3c, column 4), suggesting the CO₂ feedstock is the key to the generation of CO (Fig. 3c, column 1). In addition, the cycling stability of TCN(NH₃) calcined under NH₃ at a flow rate of 200 mL/min is tested, and the results are presented in Fig. 3d. Photocatalytic CO₂ reduction activity is maintained at 100 μmol g⁻¹ h⁻¹ over five cycles. During cycling, once additional triethanolamine (TEOA, 2 mL) has been added to the reaction, the product generation rate is stabilized. The SEM, XRD and FTIR analyses in Fig. S8–S10 further demonstrate that the g-C₃N₄ nanotube structure does not change during photoreduction cycling, demonstrating its photostability [67,68]. The most reported photocatalysts (such as P25-TiO₂, BP, BN and carbon) are also selected for comparison with TCN (NH₃). The results in Fig. 4c indicate that the CO₂ reduction

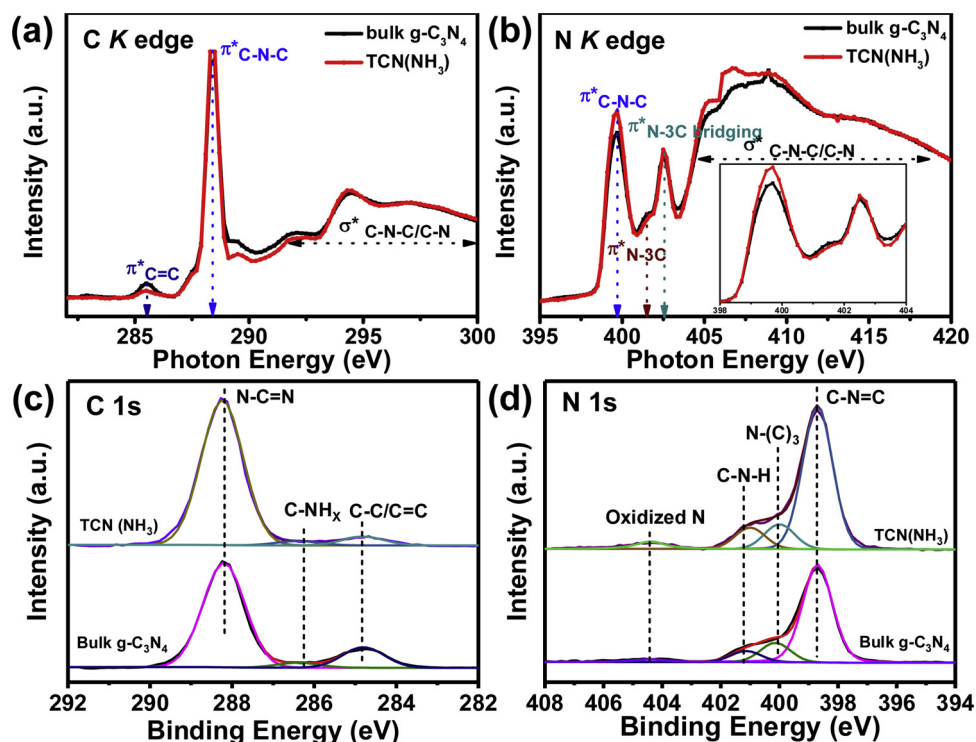


Fig. 2. Synchrotron radiation XANES and XPS measurements. (a) C K-edge and (b) N K-edge XANES spectra and (c) C 1s and (d) N 1s XPS spectra of TCN(NH₃) and bulk g-C₃N₄.

performance of TCN(NH₃) (103.6 $\mu\text{mol g}^{-1} \text{h}^{-1}$) is obviously higher than that of P25-TiO₂ (7.1 $\mu\text{mol g}^{-1} \text{h}^{-1}$), BP (7.9 $\mu\text{mol g}^{-1} \text{h}^{-1}$), BN (0 $\mu\text{mol g}^{-1} \text{h}^{-1}$) and carbon (0 $\mu\text{mol g}^{-1} \text{h}^{-1}$), and the CO₂ reduction performance of TCN(NH₃) is also higher than most reported g-C₃N₄-based photocatalysts (Table S6). The quantum efficiency (QE) of TCN(NH₃) is 0.43% at 400 nm (Fig. S11), which is also higher than that of most carbon nitrogen-based materials for CO₂ photocatalytic reduction

(Table S6). The QE decreased quickly at longer wavelengths, achieving 0.26%, 0.00013% and 0% at 420, 435 and 450 nm, respectively.

2.3. Mechanism and structure-activity relationship analysis

The excellent activity of TCN(NH₃) can be ascribed to the 1D porous tubular structure and abundant amino groups. First, the one-

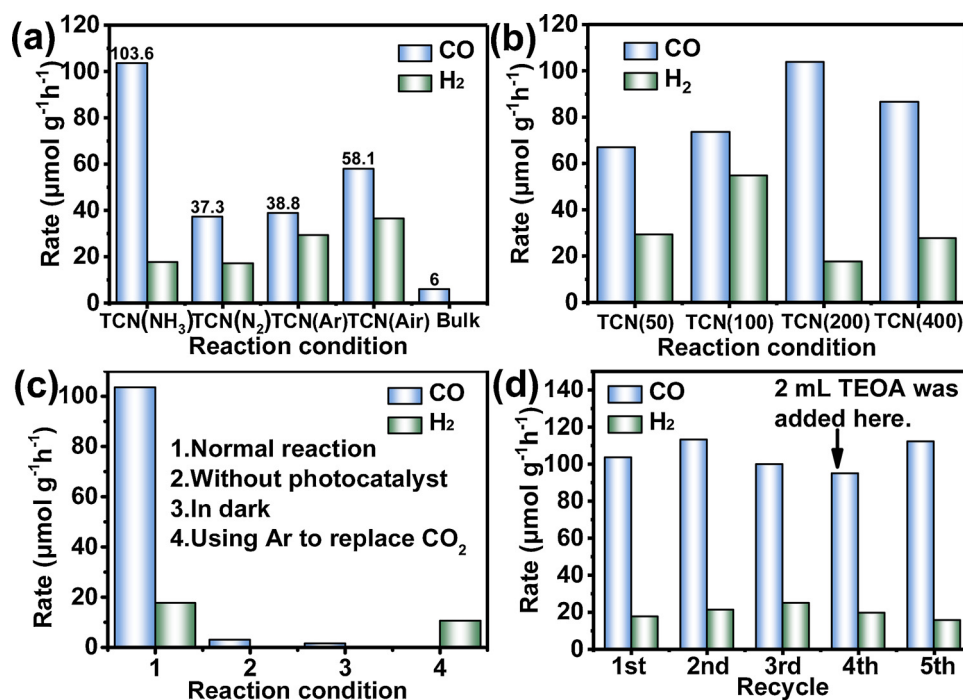


Fig. 3. Photocatalytic CO₂ reduction activity under visible light irradiation. (a, b) CO₂ photoreduction activities of different samples, (c) CO₂ reduction performance under various conditions and (d) formation of CO/H₂ in stability tests.

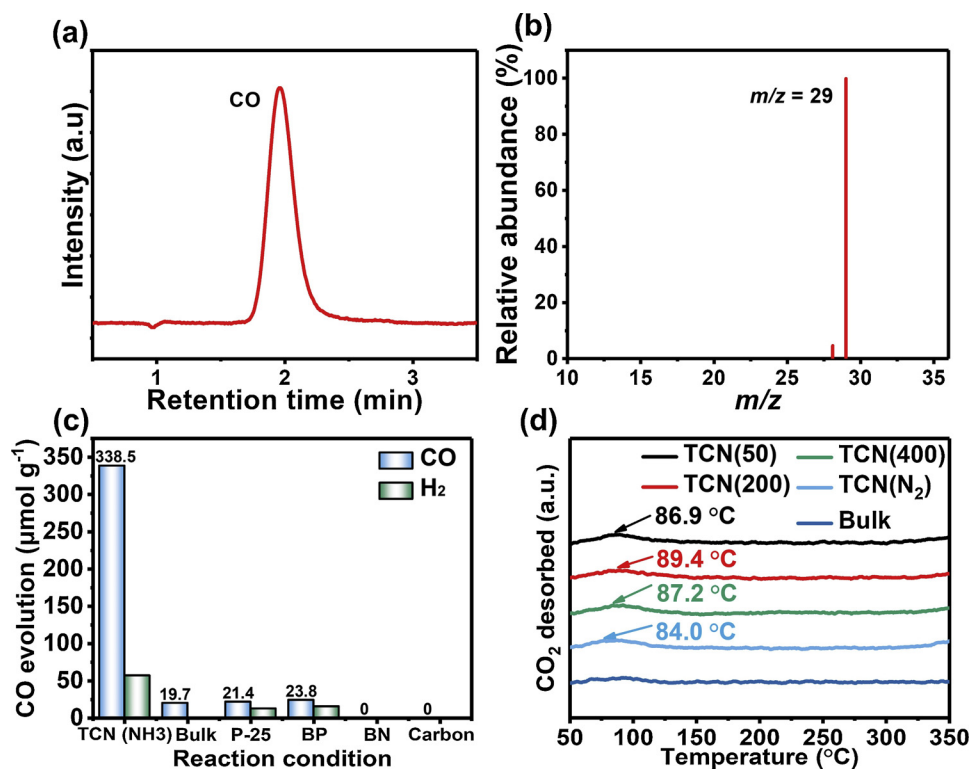


Fig. 4. GC-MS analysis of the CO generated from the $^{13}\text{CO}_2$ isotope experiments and photocatalytic CO_2 performance. (a) GC spectrum, (b) MS spectrum, (c) generation of CO over different catalysts under visible light irradiation for 3 h and (d) CO_2 -TPD patterns of the various TCN catalysts.

dimensional porous tubular structure can greatly increase the surface area and promote optical absorption because of the reflection of incident light, leading to rapid and long-distance electron transport. Furthermore, as shown in Table S1–S4 and Fig. 2, the N contents of TCN (NH_3) are clearly higher than that of TCN(air), TCN(Ar) and TCN(N_2). The amino groups are hole stabilizers, extending the lifetime of the photogenerated charge [48]. Simultaneously, the strong Lewis basicity of the amino groups is beneficial to the capture of CO_2 by forming hydrogen bonds with CO_2 . Therefore, TCN(NH_3) has the stronger adsorption of CO_2 than bulk g- C_3N_4 and TCN synthesized in different atmosphere (Air, Ar, N_2), which facilitates the photocatalytic reduction reaction [15,38–45]. To illustrate the effect of amino groups on the adsorption of CO_2 and desorption of CO, density functional theory (DFT) calculations were performed to determine the energy required for the adsorption of CO_2 and desorption of CO. Fig. 5a shows the CO_2 adsorption energies and the CO desorption energies of TCN with or without amino modification. Based on the literature, CO_2 adsorption occurs via O-terminated adsorption. Therefore, TCN(NH_3) may have stronger CO_2 adsorption performance than that of TCN without amino modification because the modified amino groups can form hydrogen bonds with CO_2 [69]. The DFT calculations validated this hypothesis. TCN(NH_3) has a higher CO_2 adsorption energy (-0.358 eV) than TCN without amino modification. The N–H...O separation in TCN(NH_3) is 2.445 Å, which is within the range of hydrogen bonding interactions. This hydrogen bonding interaction may be key to enhancing the CO_2 adsorption energy. In addition, the desorption of the generated CO molecules is another important step for CO_2 photoreduction. As shown in Fig. 5b, the CO adsorption model involves C-terminated adsorption, and the CO desorption energy (0.032 eV) in TCN(NH_3) is smaller than that of TCN (0.148 eV), which may be because the N–H...C interaction is weaker than the N–H...O interaction. Thus, TCN(NH_3) is beneficial for the release of CO from the nanotubes. Based on the above DFT calculations, TCN(NH_3) not only enhances the CO_2 adsorption energy but also decreases the CO desorption energy, which could ultimately lead to better photocatalytic CO_2 reduction activity.

The main reasons for the increase and subsequent decrease in activity for the catalysts synthesized using different NH_3 flow rates are now given. (1) As the flow rate of NH_3 increased to a certain range (200 mL/min), the BET surface area of the TCN(NH_3) sample gradually increased to 135.8 m 2 /g (Table S5), which is important for the adsorption of CO_2 . To understand the interactions between CO_2 and the photocatalyst surfaces, the temperature programmed desorption (TPD)- CO_2 profiles of the different photocatalysts are presented in Fig. 4d. Compared to those of the TCN(NH_3) samples calcined at different NH_3 flow rates, TCN(N_2) calcined under N_2 at 200 mL/min exhibits CO_2 desorption at the lowest temperature (84.0 °C), suggesting fewer interactions between CO_2 and TCN(N_2). In contrast, TCN(NH_3) calcined under NH_3 at 200 mL/min shows CO_2 desorption at the highest temperature (89.4 °C), indicating that there are a large number of interactions with CO_2 . In other words, TCN(200) has the strongest adsorption of CO_2 . The above results correspond to the observed photocatalytic performance shown in Fig. 3a, b. (2) For the sample prepared with an NH_3 flow rate of 400 mL/min, the CO production rate decreases to 86.5 $\mu\text{mol g}^{-1} \text{h}^{-1}$. The increased NH_3 flow rate increased the exfoliation of the g- C_3N_4 nanotubes. As shown in Fig. S4 and S12, the tube wall of TCN becomes thinner gradually with the increase of NH_3 flow rate, and finally collapsing when the flow rate reaches 400 mL/min (Fig. S12c, d). This eventually results in a decrease in photocatalytic activity.

The light absorption and separation efficiency of photogenerated charges are also the key factors for photocatalytic activity [70,71]. A significantly reduced photoluminescence emission intensity of TCN (NH_3) is observed in contrast with that of bulk g- C_3N_4 , indicating a lower recombination rate of charge carriers in TCN(NH_3) (Fig. S13) [72]. The improved photocharge could be further quantified based on the decreased electrochemical impedance and the increased photocurrent (Fig. S13c–e) of TCN(NH_3) electrodes. As shown in Fig. S13c, d, TCN(NH_3) has the higher photocurrent density than that of bulk g- C_3N_4 , TCN(air), TCN(Ar) and TCN(N_2), which may be due to the more efficient charge separation efficiency of TCN(NH_3) [73,74]. TCN(NH_3)

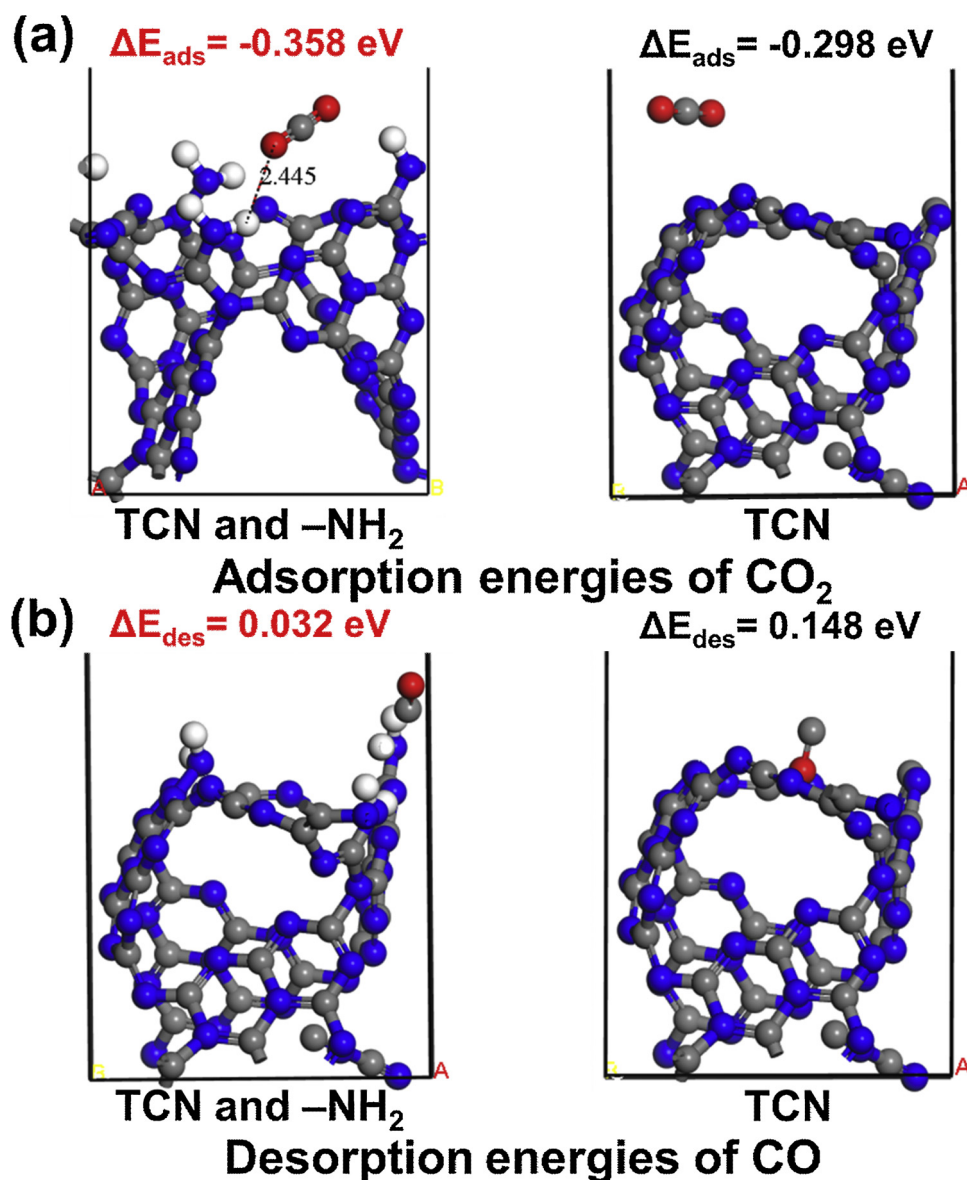


Fig. 5. (a) Adsorption energies of CO_2 and (b) desorption energies of CO on various TCN catalysts (all results obtained from first-principles calculations).

exhibits the smaller arc radius than that of bulk $g\text{-C}_3\text{N}_4$ (Fig. S13e), which corresponds to lower resistance and higher charge separation efficiency [75].

Based on the above experimental results, as well as the catalyst characterization, the excellent photocatalytic activity of $\text{TCN}(\text{NH}_3)$ is attributed to the following: first, $\text{TCN}(\text{NH}_3)$ has a unique 1D tubular structure, which can maximize $\text{TCN}(\text{NH}_3)$ exposure to sunlight and increase the light utilization because of the multiple reflections of incident light in the tubular structure. Meanwhile, the larger specific surface area of $\text{TCN}(\text{NH}_3)$ can provide more photocatalytic reaction centers for photocatalytic reduction [76]. Secondly, the introduction of amino groups effectively enhances the Lewis basicity and hydrophilicity, which can enhance the photocatalytic performance. The 1D tubular structure and the introduction of amino groups are conducive to increasing the adsorption of CO_2 and the charge separation/transfer during catalytic reaction, resulting in a smaller interfacial charge transfer resistance and a higher charge separation/transfer efficiency.

3. Conclusions

In summary, porous nitrogen-rich $g\text{-C}_3\text{N}_4$ nanotubes ($\text{TCN}(\text{NH}_3)$)

are synthesized through a molecular self-assembly strategy yielding highly efficient and stable metal-free catalysts for visible-light-driven photocatalytic CO_2 reduction. The CO production rates of $\text{TCN}(\text{NH}_3)$ are 17, 15 and 13 times higher than those of individual carbon nitride, P25 and BP, respectively. The unique porous nanotube structure and nitrogen-rich features of the $\text{TCN}(\text{NH}_3)$ catalysts facilitate light capture via multiple reflections, as well as the adsorption of CO_2 and desorption of CO, which increase the photocatalytic CO_2 reduction activity. Thus, this work provides direction for the design and synthesis of low cost and nature-inspired metal-free materials for photocatalytic CO_2 conversion.

Acknowledgements

This study was supported by National Nature Science Foundation of China (21676128, 21776118), A Project Funded by the Priority Academic Program Development of Jiangsu Higher Education Institutions, High-tech Research Key laboratory of Zhenjiang (SS2018002) and the high performance computing platform of Jiangsu University.

Appendix A. Supplementary data

Supplementary material related to this article can be found, in the online version, at doi:<https://doi.org/10.1016/j.apcatb.2019.117854>.

References

- [1] S. Sorcar, J. Thompson, Y. Hwang, Y.H. Park, T. Majima, C.A. Grimes, J.R. Durrant, S.-I. In, *Energy Environ. Sci.* 11 (2018) 3183–3193.
- [2] H. Rao, L.C. Schmidt, J. Bonin, M. Robert, *Nature* 548 (2017) 74–77.
- [3] Y.X. Pan, Y. You, S. Xin, Y. Li, G. Fu, Z. Cui, Y.L. Men, F.F. Cao, S.H. Yu, J.B. Goodenough, *J. Am. Chem. Soc.* 139 (2017) 4123–4129.
- [4] Y. Wu, Y. Wei, Q. Guo, H. Xu, L. Gu, F. Huang, D. Luo, Y. Huang, L. Fan, J. Wu, *Solar Energy Mater. Solar Cells* 176 (2018) 230–238.
- [5] Z. Jiang, H. Sun, T. Wang, B. Wang, W. Wei, H. Li, S. Yuan, T. An, H. Zhao, J. Yu, P.K. Wong, *Energy Environ. Sci.* 11 (2018) 2382–2389.
- [6] X. Zhu, H. Ji, J. Yi, J. Yang, X. She, P. Ding, L. Li, J. Deng, J. Qian, H. Xu, H. Li, *Ind. Eng. Chem. Res.* 57 (2018) 17394–17400.
- [7] J. Zhang, Y. Gao, X. Jia, J. Wang, Z. Chen, Y. Xu, *Solar Energy Mater. Solar Cells* 182 (2018) 113–120.
- [8] B. Wang, J. Di, L. Lu, S. Yan, G. Liu, Y. Ye, H. Li, W. Zhu, H. Li, J. Xia, *Appl. Catal. B* 254 (2019) 551–559.
- [9] S. Wang, B.-Y. Guan, Y. Lu, X.W.D. Lou, *J. Am. Chem. Soc.* 139 (2017) 17305–17308.
- [10] S. Qamar, F. Lei, L. Liang, S. Gao, K. Liu, Y. Sun, W. Ni, Y. Xie, *Nano Energy* 26 (2016) 692–698.
- [11] K. Cho, K. Kim, K. Park, C. Kim, S. Kim, A. Al-Saggaf, I. Gereige, H. Jung, *ACS Catal.* 7 (2017) 7064–7069.
- [12] D. Voiry, H.S. Shin, K.P. Loh, M. Chhowalla, *Nat. Rev. Chem.* 2 (2018) 0105.
- [13] H. Xie, T. Wang, J. Liang, Q. Li, S. Sun, *Nano Today* 21 (2018) 41–54.
- [14] H. Shi, G. Chen, C. Zhang, Z. Zou, *ACS Catal.* 4 (2014) 3637–3643.
- [15] Z. Sun, H. Wang, Z. Wu, L. Wang, *Catal. Today* 300 (2018) 160–172.
- [16] J.Y. Liu, H. Xu, Y.G. Xu, Y.H. Song, J.B. Lian, Y. Zhao, L. Wang, L.Y. Huang, H.Y. Ji, H.M. Li, *Appl. Catal. B* 207 (2017) 429–437.
- [17] X. Meng, L. Liu, S. Ouyang, H. Xu, D. Wang, N. Zhao, J. Ye, *Adv. Mater.* 28 (2016) 6811–6803.
- [18] Q. Hao, Y. Song, Z. Mo, S. Mishra, J. Pang, Y. Liu, J. Lian, J. Wu, S. Yuan, H. Xu, H. Li, *ACS Sustain. Chem. Eng.* 7 (2018) 3234–3242.
- [19] F. Guo, P. Yang, Z. Pan, X.N. Cao, Z. Xie, X. Wang, *Angew. Chem. Int. Ed.* 56 (2017) 8231–8235.
- [20] F. Chen, H. Huang, L. Ye, T. Zhang, Y. Zhang, X. Han, T. Ma, *Adv. Funct. Mater.* 28 (2018) 1804284.
- [21] J. Di, C. Zhu, M. Ji, M. Duan, R. Long, C. Yan, K. Gu, J. Xiong, Y. She, J. Xia, H. Li, Z. Liu, *Angew. Chem. Int. Ed.* 57 (2018) 14847–14851.
- [22] J. Yang, X. Zhu, Z. Mo, J. Yi, J. Yan, J. Deng, Y. Xu, Y. She, J. Qian, H. Xu, H. Li, *Inorg. Chem. Front.* 5 (2018) 3163–3169.
- [23] Z. Tong, D. Yang, Y. Sun, Y. Nan, Z. Jiang, *Small* 12 (2016) 4093–4101.
- [24] Z. Mo, H. Xu, Z. Chen, X. She, Y. Song, J. Wu, P. Yan, L. Xu, Y. Lei, S. Yuan, H. Li, *Appl. Catal. B* 225 (2018) 154–161.
- [25] D.P. Goronzy, M. Ebrahimi, F. Rosei, Y. Arramel, S. Fang, S.L. De Feyter, S.L. Tait, C. Wang, P.H. Beton, A.T.S. Wee, P.S. Weiss, D.F. Perepichka, *ACS Nano* 12 (2018) 7445–7481.
- [26] Y. Liu, L. Wang, H. Feng, X. Ren, J. Ji, F. Bai, H. Fan, *Nano Lett.* 19 (2019) 2614–2619.
- [27] L. Zhang, N. Ding, L. Lou, K. Iwasaki, H. Wu, Y. Luo, D. Li, K. Nakata, A. Fujishima, Q. Meng, *Adv. Funct. Mater.* 29 (2019) 1806774.
- [28] N. Tian, K. Xiao, Y. Zhang, X. Lu, L. Ye, P. Gao, T. Ma, H. Huang, *Appl. Catal. B* 253 (2019) 196–205.
- [29] Y. Guo, J. Li, Y. Yuan, L. Li, M. Zhang, C. Zhou, Z. Lin, *Angew. Chem. Int. Ed.* 55 (2016) 14693–14697.
- [30] M. Shalom, S. Inal, C. Fettkenhauer, D. Neher, M. Antonietti, *J. Am. Chem. Soc.* 135 (2013) 7118–7121.
- [31] Y. Jun, E. Lee, X. Wang, W. Hong, G. Stucky, A. Thomas, *Adv. Funct. Mater.* 23 (2013) 3661–3667.
- [32] J. Xu, H. Wang, C. Zhang, X. Yang, S. Cao, J. Yu, M. Shalom, *Angew. Chem. Int. Ed.* 56 (2017) 8426–8430.
- [33] M. Shalom, S. Gimenez, F. Schipper, I. Herraiz-Cardona, J. Bisquert, M. Antonietti, *Angew. Chem. Int. Ed.* 53 (2014) 3654–3658.
- [34] M. Shalom, M. Guttentag, C. Fettkenhauer, S. Inal, D. Neher, A. Llobet, M. Antonietti, *Chem. Mater.* 26 (2014) 5812–5818.
- [35] Y. Liao, S. Zhu, J. Ma, Z. Sun, C. Yin, C. Zhu, X. Lou, D. Zhang, *ChemCatChem* 6 (2014) 3419–3425.
- [36] Y. Ishida, L. Chabanne, M. Antonietti, M. Shalom, *Langmuir* 30 (2014) 447–451.
- [37] S. Guo, Z. Deng, M. Li, B. Jiang, C. Tian, Q. Pan, H. Fu, *Angew. Chem. Int. Ed.* 55 (2016) 1830–1834.
- [38] S. Liu, H. Yang, X. Huang, L. Liu, W. Cai, J. Gao, X. Li, T. Zhang, Y. Huang, B. Liu, *Adv. Funct. Mater.* 28 (2018) 1800499.
- [39] Y. Chen, M. Wang, Y. Ma, Y. Li, J. Cai, Z. Li, *Catal. Sci. Technol.* 8 (2018) 2218–2223.
- [40] H. Park, J.H. Lee, E.H. Kim, K.Y. Kim, Y.H. Choi, D.H. Youn, J.S. Lee, *Chem. Commun.* 52 (2016) 14302–14305.
- [41] Y. Bao, C. Huang, L. Chen, Y. Zhang, L. Liang, J. Wen, M. Fu, J. Wu, D. Ye, *J. Energy Chem.* 27 (2018) 381–388.
- [42] Y. Dong, K.K. Ghuman, R. Popescu, P.N. Duchesne, W. Zhou, J.Y.Y. Loh, A.A. Jelle, J. Jia, D. Wang, X. Mu, C. Kubel, L. Wang, L. He, M. Ghoussoub, Q. Wang, T.E. Wood, L.M. Reyes, P. Zhang, N.P. Kherani, C.V. Singh, G.A. Ozin, *Adv. Sci.* 5 (2018) 1700732.
- [43] Z. Huang, F. Li, B. Chen, T. Lu, Y. Yuan, G. Yuan, *Appl. Catal. B* 136–137 (2013) 269–277.
- [44] D.W. Stephan, *Acc. Chem. Res.* 48 (2015) 306–316.
- [45] D.W. Stephan, G. Erker, *Angew. Chem. Int. Ed.* 54 (2015) 6400–6441.
- [46] Q. Han, Z. Cheng, B. Wang, H. Zhang, L. Qu, *ACS Nano* 12 (2018) 5221–5227.
- [47] H. Pan, Y.-W. Zhang, V.B. Shenoy, H. Gao, *ACS Catal.* 1 (2011) 99–104.
- [48] N. Meng, J. Ren, Y. Liu, Y. Huang, T. Petit, B. Zhang, *Energy Environ. Sci.* 11 (2018) 566–571.
- [49] Q. Tay, P. Kanhere, C.F. Ng, S. Chen, S. Chakraborty, A.C.H. Huan, T.C. Sum, R. Ahuja, Z. Chen, *Chem. Mater.* 27 (2015) 4930–4933.
- [50] X. Yang, L. Tian, X. Zhao, H. Tang, Q. Liu, G. Li, *Appl. Catal. B* 244 (2019) 240–249.
- [51] X. She, J. Wu, J. Zhong, H. Xu, Y. Yang, R. Vajtai, J. Lou, Y. Liu, D. Du, H. Li, P.M. Ajayan, *Nano Energy* 27 (2016) 138–146.
- [52] Q. Liu, J. Shen, X. Yu, X. Yang, W. Liu, J. Yang, H. Tang, H. Xu, H. Li, Y. Li, J. Xu, *Appl. Catal. B* 248 (2019) 84–94.
- [53] H. Xu, J. Yi, X. She, Q. Liu, L. Song, S. Chen, Y. Yang, Y. Song, R. Vajtai, J. Lou, H. Li, S. Yuan, J. Wu, P.M. Ajayan, *Appl. Catal. B* 220 (2018) 379–385.
- [54] Z. Mo, H. Xu, Z. Chen, X. She, Y. Song, J. Lian, X. Zhu, P. Yan, Y. Lei, S. Yuan, H. Li, *Appl. Catal. B* 241 (2019) 452–460.
- [55] Y. Wang, M.K. Bayazit, S.J.A. Moniz, Q. Ruan, C.C. Lau, N. Martsinovich, J. Tang, *Energy Environ. Sci.* 10 (2017) 1643–1651.
- [56] D.J. Martin, K. Qiu, S.A. Shevlin, A.D. Handoko, X. Chen, Z. Guo, J. Tang, *Angew. Chem. Int. Ed.* 53 (2014) 9240–9245.
- [57] S. Cao, H. Chen, F. Jiang, X. Wang, *Appl. Catal. B* 224 (2018) 222–229.
- [58] P. Xia, B. Zhu, J. Yu, S. Cao, M. Jaroniec, *J. Mater. Chem. A* 5 (2017) 3230–3238.
- [59] W. Zhang, G. Li, W. Wang, Y. Qin, T. An, X. Xiao, W. Choi, *Appl. Catal. B* 232 (2018) 11–18.
- [60] R. Zhang, H. Wang, S. Tang, C. Liu, F. Dong, H. Yue, B. Liang, *ACS Catal.* 8 (2018) 9280–9286.
- [61] H. Zai, Y. Zhao, S. Chen, L. Ge, C. Chen, Q. Chen, Y. Li, *Nano Res.* 11 (2018) 2544–2552.
- [62] J. Lee, J. Ryu, J. Kim, S. Nam, J. Han, T. Lim, S. Gautam, K. Chae, C. Yoon, *J. Mater. Chem. A* 2 (2014) 9490.
- [63] G.P. Mane, S.N. Talapaneni, K.S. Lakhi, H. Ilbeygi, U. Ravon, K. Al-Bahily, T. Mori, D.H. Park, A. Vinu, *J. Am. Chem. Soc.* 56 (2017) 8481–8485.
- [64] Z. Wei, M. Liu, Z. Zhang, W. Yao, H. Tan, Y. Zhu, *Energy Environ. Sci.* 11 (2018) 2581–2589.
- [65] Y. Wang, W. Yang, X. Chen, J. Wang, Y. Zhu, *Appl. Catal. B* 220 (2018) 337–347.
- [66] N. Sagara, S. Kamimura, T. Tsubota, T. Ohno, *Appl. Catal. B* 192 (2016) 193–198.
- [67] Q. Liu, J. Shen, X. Yang, T. Zhang, H. Tang, *Appl. Catal. B* 232 (2018) 562–573.
- [68] X.W. Zhu, J.M. Yang, X.J. She, Y.H. Song, J.C. Qian, Y. Wang, H. Xu, H.M. Li, Q.Y. Yan, *J. Mater. Chem. A* 7 (2019) 5209–5213.
- [69] G. Hu, Z. Wu, S. Dai, D.E. Jiang, *ACS Appl. Mater. Interfaces* 10 (2018) 6694–6700.
- [70] J.J. Yi, H.P. Li, Y.J. Gong, X.J. She, Y.H. Song, Y.G. Xu, J.J. Deng, S.Q. Yuan, H. Xu, H.M. Li, *Appl. Catal. B* 243 (2019) 330–336.
- [71] P. Yan, D. Jiang, Y. Tian, L. Xu, J. Qian, H. Li, J. Xia, H. Li, *Biosens. Bioelectron.* 111 (2018) 74–81.
- [72] Y. Lu, X. Cheng, G. Tian, H. Zhao, L. He, J. Hu, S. Wu, Y. Dong, G. Chang, S. Lenaerts, S. Siffert, G. Van Tendeloo, Z. Li, L. Xu, X. Yang, B. Su, *Nano Energy* 47 (2018) 8–17.
- [73] S. Huang, Y. Xu, T. Zhou, M. Xie, Y. Ma, Q. Liu, L. Jing, H. Xu, H. Li, *Appl. Catal. B* 225 (2018) 40–50.
- [74] P. Yan, D. Jiang, H. Li, J. Bao, L. Xu, J. Qian, C. Chen, J. Xia, *Sens. Actuators B* 279 (2019) 466–475.
- [75] J.Y. Liu, H. Xu, H.P. Li, Y.H. Song, J.J. Wu, Y.J. Gong, L. Xu, S.Q. Yuan, H.M. Li, P.M. Ajayan, *Appl. Catal. B* 243 (2019) 151–160.
- [76] X. She, H. Xu, Y. Yu, L. Li, X. Zhu, Z. Mo, Y. Song, J. Wu, S. Yuan, H. Li, *Small* 15 (2019) 1804613.